



A New Mechanism of Electric Dipole Spin Resonance: Hyperfine Coupling in Quantum Dots

Citation

Laird, Edward A., Christian Barthel, Emmanuel Rashba, Charles M. Marcus, M. P. Hanson, and Arthur C. Gossard. 2009. A new mechanism of electric dipole spin resonance: hyperfine coupling in quantum dots. *Semiconductor Science and Technology* 24(064004).

Published Version

doi:10.1088/0268-1242/24/6/064004

Permanent link

<http://nrs.harvard.edu/urn-3:HUL.InstRepos:5110753>

Terms of Use

This article was downloaded from Harvard University's DASH repository, and is made available under the terms and conditions applicable to Open Access Policy Articles, as set forth at <http://nrs.harvard.edu/urn-3:HUL.InstRepos:dash.current.terms-of-use#OAP>

Share Your Story

The Harvard community has made this article openly available.
Please share how this access benefits you. [Submit a story](#).

[Accessibility](#)

A new mechanism of electric dipole spin resonance: hyperfine coupling in quantum dots

**E A Laird¹, C Barthel¹, E I Rashba^{1,2}, C M Marcus¹,
M P Hanson³ and A C Gossard³**

¹ Department of Physics, Harvard University, Cambridge, Massachusetts 02138, USA

² Center for Nanoscale Systems, Harvard University, Cambridge, Massachusetts 02138, USA

³ Materials Department, University of California at Santa Barbara, Santa Barbara, California 93106, USA

E-mail: marcus@harvard.edu

Abstract. A recently discovered mechanism of electric dipole spin resonance, mediated by the hyperfine interaction, is investigated experimentally and theoretically. The effect is studied using a spin-selective transition in a GaAs double quantum dot. The resonant frequency is sensitive to the instantaneous hyperfine effective field, revealing a nuclear polarization created by driving the resonance. A device incorporating a micromagnet exhibits a magnetic field difference between dots, allowing electrons in either dot to be addressed selectively. An unexplained additional signal at half the resonant frequency is presented.

PACS numbers: 76.20.+q, 76.30.-v, 76.70.Fz, 78.67.Hc

Submitted to: *Semicond. Sci. Technol.*

1. Introduction

Electric dipole spin resonance (EDSR) is a method to electrically manipulate electron spins. In this technique, two fields are applied; a static magnetic field \mathbf{B} and an oscillating electric field $\tilde{\mathbf{E}}(t)$ resonant with the electron precession (Larmor) frequency [1, 2, 3, 4]. Spin resonance techniques are of interest for quantum computing schemes based on single electron spins, because they allow arbitrary one-qubit operations [5]. Single-spin EDSR is a particularly desirable experimental tool because it allows spin manipulation without time-dependent magnetic fields, which are difficult to generate and localize at the nanoscale [6, 7, 8, 9].

Achieving EDSR requires a mechanism to couple $\tilde{\mathbf{E}}$ to the electron spin σ . This coupling can be achieved by the traditional spin-orbit interaction, which couples σ to the electron momentum \mathbf{k} , or by an inhomogeneous Zeeman interaction, which couples σ to the electron coordinate \mathbf{r} [10, 4, 11, 12, 13]. Single-spin EDSR has recently been achieved in quantum dots using both techniques [14, 15].

Recently, we presented an experimental and theoretical study of a novel EDSR effect mediated by the spatial inhomogeneity of the hyperfine nuclear field [16]. An electron moving under the influence of the electric field $\tilde{\mathbf{E}}(t)$ experiences this inhomogeneity as an oscillating hyperfine coupling which drives spin transitions. In this paper, we illuminate the underlying physics and present new experimental data on a still unexplained phenomenon at half the resonant frequency.

This EDSR effect is observed via spin-blocked transitions in a few-electron GaAs double quantum dot [17]. As expected for a hyperfine mechanism, but in contrast to the $\mathbf{k} - \sigma$ -coupling mediated EDSR, the resonance strength is independent of \mathbf{B} at low field and shows, when averaged over nuclear configurations, no Rabi oscillations as a function of time. We find that at large \mathbf{B} driving the resonance creates a nuclear polarization, which we interpret as the backaction of EDSR on the nuclei [18, 19, 9, 20, 21]. Finally, we demonstrate that spins can be individually addressed in each dot by creating a local field gradient.

2. Device and measurement

The device for which most data is presented (Figure 1(a)) was fabricated on a GaAs/Al_{0.3}Ga_{0.7}As heterostructure with two-dimensional electron gas (2DEG) of density $2 \times 10^{15} \text{ m}^{-2}$ and mobility $20 \text{ m}^2/\text{Vs}$ located 110 nm below the surface. Voltages applied to Ti/Au top gates locally deplete the 2DEG, defining a few-electron double quantum dot. A nearby charge sensing quantum point contact (QPC) is sensitive to the electron occupation (N_L, N_R) of the left (N_L) and right (N_R) dots [22, 23]. The voltages V_L and V_R on gates L and R can be rapidly pulsed; in addition, L is coupled to a microwave source. The static magnetic field \mathbf{B} was applied in the plane of the heterostructure, and measurements were performed in a dilution refrigerator at 150 mK electron temperature.

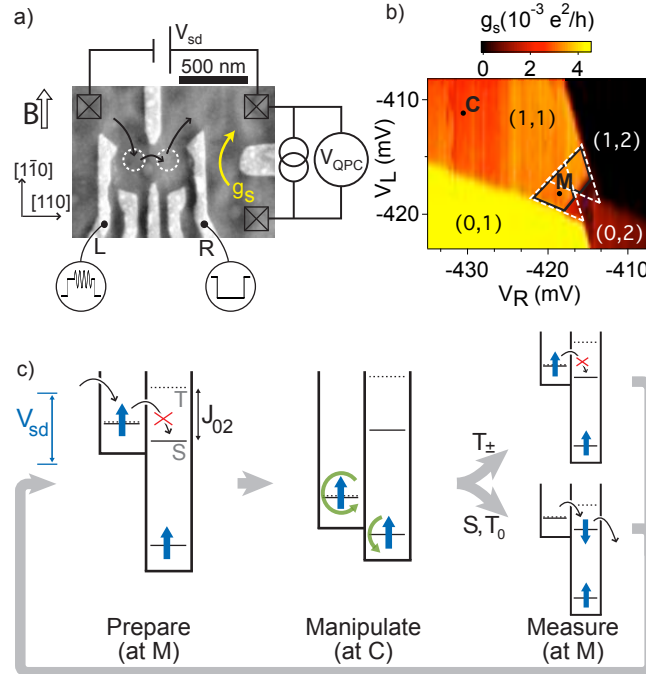


Figure 1. (a) Micrograph of a device lithographically identical to the one measured, with schematic of the measurement circuit. Quantum dot locations are shown by dashed circles, and a bias V_{sd} drives sequential tunneling in the direction marked by black arrows. The conductance g_s of the QPC on the right is sensitive to the dot occupation. The direction of the magnetic field \mathbf{B} and the crystal axes are indicated. (b) QPC conductance g_s measured at $V_{sd} \sim 600 \mu\text{eV}$ near the (1,1)-(0,2) transition. Equilibrium occupations for different gate voltages are shown, as are gate voltage configurations during the measurement/reinitialization (M) and manipulation (C) pulses. The two white dashed triangles outline regions where transport is not Coulomb blocked; the solid black line outlines where spin blockade is active. A plane background has been subtracted. (c) Energy levels of the double dot during the pulse cycle (See text).

The characteristic feature of tunnel-coupled quantum dots is a discrete electron energy spectrum. An overall shift to the spectrum, proportional to the electron occupation, is induced by V_L and V_R , which therefore determine which occupation is energetically favoured. Figure 1(b) shows the QPC conductance g_s as a function of V_L and V_R ; different conductances correspond to different (N_L, N_R) . For most V_L, V_R configurations, only one value of (N_L, N_R) is energetically accessible; these correspond in Figure 1(b) to regions of uniform g_s .

A bias V_{sd} applied across the device drives electron transport via sequential tunneling subject to two constraints [24]. The first constraint, Coulomb blockade, arises because for most gate configurations electrostatic repulsion prevents additional electrons from tunneling onto either dot. This constraint inhibits transport except when V_L, V_R are tuned so that three occupation configurations are near-degenerate. The energy cost of an extra electron tunneling through the device is then small enough to be provided by the bias voltage. Values of V_L and V_R satisfying this condition correspond to the two white

dashed triangular regions marked in Figure 1(b), for which transport is permitted via the transition sequences $(0, 2) \rightarrow (0, 1) \rightarrow (1, 1) \rightarrow (0, 2)$ or $(0, 2) \rightarrow (1, 2) \rightarrow (1, 1) \rightarrow (0, 2)$.

A second constraint, spin blockade, is caused by the Pauli exclusion principle, which leads to an intra-dot exchange energy J_{02} in the right dot [25, 26]. As shown in the first panel of Figure 1(c), the effect of this exchange is to make the $(1, 1) \rightarrow (0, 2)$ transition selective in the two-electron spin state, inhibited for triplet states but allowed for the singlet. Although the hyperfine field difference between dots rapidly converts the $m_s = 0$ component T_0 of the blocked triplet T to an unblocked singlet S , decay of $m_s = \pm 1$ components T_{\pm} requires a spin flip and therefore proceeds much more slowly. This spin flip becomes the rate-limiting step in transport, and so the time-averaged occupation is dominated by the $(1,1)$ portion of the transport sequence [26]. Gate configurations where spin blockade applies correspond to the black solid outlined region of Figure 1(b); inside this region, g_s has the value corresponding to $(1,1)$. Any process that induces spin flips will partially break spin blockade and lead to a decrease in g_s .

Unless stated otherwise, EDSR is detected via changes in g_s while the following cycle of voltage pulses V_L and V_R [9] is applied to L and R (Figure 1(c)). The cycle begins inside the spin blockade region (M in Figure 1(b)), so that the two-electron state is initialized to $(1, 1)T_{\pm}$ with high probability. A $\sim 1 \mu\text{s}$ pulse to point C prevents electron tunneling regardless of spin state. Towards the end of this pulse, a microwave burst of duration τ_{EDSR} at frequency f is applied to gate L. Finally the system is brought back to M for $\sim 3 \mu\text{s}$ for readout/reinitialization. If and only if a spin (on either dot) was flipped during the pulse, the transition $(1, 1) \rightarrow (0, 2)$ occurs, leading to a change in average occupation and in g_s . If this transition occurs, subsequent electron transitions reinitialize the state to $(1, 1)T_{\pm}$ by the end of this step, after which the pulse cycle is repeated. This pulsed EDSR scheme has the advantage of separating spin manipulation from readout.

Changes in g_s are monitored via the voltage V_{QPC} across the QPC sensor biased at 5 nA. For increased sensitivity, the microwaves are chopped at 227 Hz and the change in voltage δV_{QPC} is synchronously detected using a lock-in amplifier. We interpret δV_{QPC} as proportional to the spin-flip probability during a microwave burst, averaged over the 100 ms lock-in time constant.

3. EDSR spectroscopy

Resonant response is seen clearly as B and f are varied for constant $\tau_{\text{EDSR}} = 1 \mu\text{s}$ (Figure 2.) A peak in δV_{QPC} , corresponding to a spin transition, is seen at a frequency proportional to B . This is the key signature of spin resonance. From the slope of the resonant line in Figure 2 a g -factor $|g| = 0.39 \pm 0.01$ is found, typical of similar GaAs devices [27, 28]. We attribute fluctuations of the resonance frequency (inset of Figure 2) to Overhauser shift caused by the time-varying hyperfine field acting on the electron spin. Their range is $\sim \pm 22 \text{ MHz}$, corresponding to a field of $\sim 4 \text{ mT}$, consistent with Overhauser fields in similar devices [29, 30, 31].

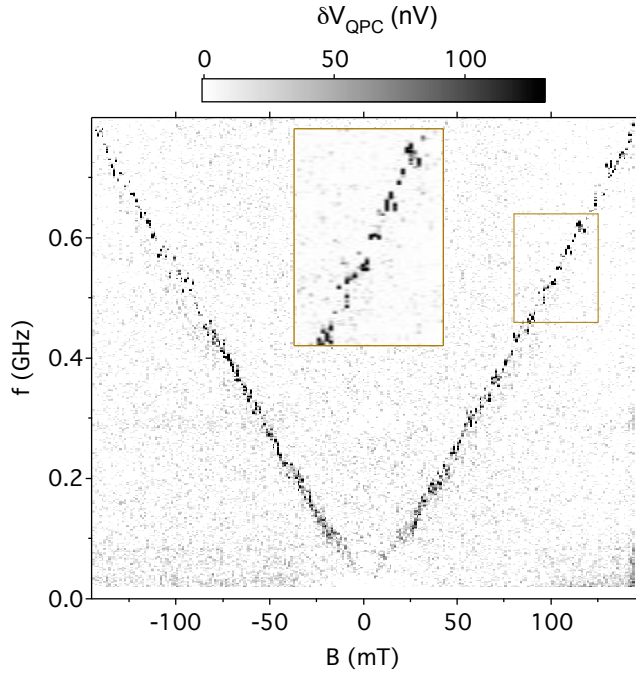


Figure 2. Signal of spin resonance δV_{QPC} as a function of magnetic field B and microwave frequency f . EDSR induces a breaking of spin blockade, which appears as a peak in the voltage across the charge sensor δV_{QPC} at the Larmor frequency. Field- and frequency-independent backgrounds have been subtracted. Inset: Jitter of resonant frequency due to random Overhauser shifts.

Information about the EDSR mechanism can be obtained by studying the peak height as a function of duration, strength, and frequency of the microwave burst (Figure 3). To reduce the effects of the shifting Overhauser field, the microwave source is frequency modulated at 3 kHz in a sawtooth pattern with depth 36 MHz about a central frequency \bar{f} . The resonance line as a function of τ_{EDSR} is shown in the inset of Figure 3(a). For equal microwave power at two different frequencies \bar{f} , the peak heights $\delta V_{\text{QPC}}^{\text{peak}}$ are plotted in Figure 3(a) (main panel). The two data sets are similar in turn-on time and saturation value; this is the case for frequencies up to $\bar{f} = 6 \text{ GHz}$. From similar data (insets of Figure 3(b)), using theory to be described, we extract the dependence of the spin-flip rate Ω_R on microwave power P_{MW} shown in the main panel of Figure 3(b). Coherent Rabi-type oscillations in $\delta V_{\text{QPC}}^{\text{peak}}(\tau_{\text{EDSR}})$ are not observed for any microwave power or magnetic field over the range measured.

The B -independence of the EDSR strength rules out spin-orbit mediated EDSR of the $\mathbf{k} - \boldsymbol{\sigma}$ type (either Dresselhaus or Rashba), for which the Rabi frequency is proportional to B [4, 13, 14]. This is in contrast to the results of [14], where the spin-orbit effect was found to dominate in a similar device to ours. A possible explanation is the device orientation relative to \mathbf{B} and the crystal axes. In both our experiment and [14], the gate geometry suggests a dominant $\tilde{\mathbf{E}}(\mathbf{t})$ oriented along one of the diagonal axes ([110] or [1 $\bar{1}$ 0]), leading to an in-plane spin-orbit effective field $\mathbf{B}_{\text{eff}}^{\text{SO}}$ perpendicular to $\tilde{\mathbf{E}}(\mathbf{t})$. In our geometry (see Figure 1(a)), this orientation of $\mathbf{B}_{\text{eff}}^{\text{SO}}$ is parallel to \mathbf{B} ,

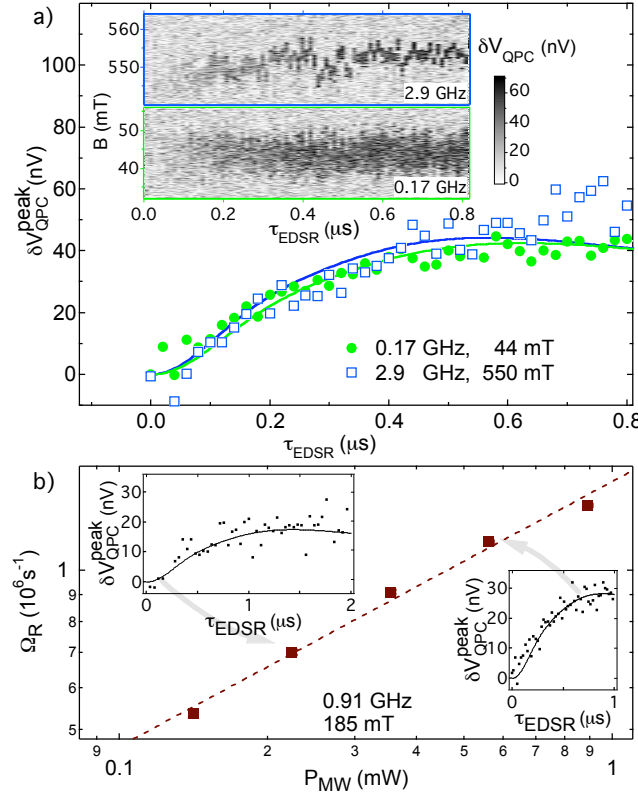


Figure 3. (a) Measured EDSR peak strength $\delta V_{QPC}^{\text{peak}}$ (symbols) versus microwave pulse duration τ_{EDSR} for two frequencies at equal power, along with theoretical fits (curves) obtained by numerically evaluating and scaling Equation (4) (see text). Inset: Raw data from which the points in the main figure are extracted. Each vertical cut corresponds to one point in the main figure. Jitter in the field position of the resonance reflects time-dependent Overhauser shifts. (b) Spin-flip rate Ω_R as a function of applied microwave power P_{MW} , along with a fit to the form $\Omega_R \propto \sqrt{P_{\text{MW}}}$ (dashed line). Insets: $\delta V_{QPC}^{\text{peak}}$ versus τ_{EDSR} for two values of the microwave power, showing the fits from which points in the main figure are derived.

and therefore ineffective at driving spin transitions. In the geometry of [14], \mathbf{B} is perpendicular to $\mathbf{B}_{\text{eff}}^{\text{SO}}$, so that the $\mathbf{k} - \boldsymbol{\sigma}$ spin-orbit mechanism becomes more efficient .

4. Theory

A theoretical description of $\delta V_{QPC}^{\text{peak}}(\tau_{\text{EDSR}})$ and its dependence on B and P_{MW} can be obtained by modeling EDSR as arising from the coupling of an electron in a single dot to an oscillating electric field $\tilde{\mathbf{E}}(t)$ and the hyperfine field of an ensemble of nuclei ‡ [16, 32]. Then the center of the dot oscillates as $\mathbf{R}(t) = -e\tilde{\mathbf{E}}(t)/m\omega_0^2$, where m is the electron effective mass, and ω_0 is its confinement frequency in a parabolic dot. As a result, the

‡ There exists some physical similarity between the hyperfine mechanism of EDSR described in this paper and EDSR due to the coupling of electron spin to a random exchange field in semimagnetic semiconductors [33].

Hamiltonian of the hyperfine coupling of the electron spin $\mathbf{S} = \boldsymbol{\sigma}/2$ to nuclear spins \mathbf{I}_j becomes time dependent, $H_{\text{hf}} = A\Sigma_j\delta(\mathbf{r} + \mathbf{R}(t) - \mathbf{r}_j)(\mathbf{I}_j \cdot \mathbf{S})$. Here A is the hyperfine coupling constant and the summation over j runs over all nuclear spins. After expanding H_{hf} in $\mathbf{R}(t)$ (assumed small compared to the dot size) and averaging over the orbital ground-state wave function $\psi_0(\mathbf{r})$ of the dot, the time dependent part of H_{hf} becomes $H_{\text{hf}}(t) = \mathbf{J}(t) \cdot \boldsymbol{\sigma}$, where $\mathbf{J}(t)$ is an operator in all \mathbf{I}_j . Choosing the z -axis in spin space along \mathbf{B} , the components of $\mathbf{J}(t)$ are $J_z = \frac{1}{2}A\sum_j\psi_0^2(\mathbf{r}_j)I_j^z$ and

$$J_{\pm}(t) = \frac{eA}{m\omega_0^2}\sum_j\psi_0(\mathbf{r}_j)\tilde{\mathbf{E}}(t) \cdot \nabla\psi_0(\mathbf{r}_j)I_j^{\pm}. \quad (1)$$

The time-dependent off-diagonal components $J_{\pm}(t)$ drive EDSR, while the quasi-static diagonal component J_z describes detuning of EDSR from the Larmor frequency ω_L by an amount ω_z randomly distributed as $\rho(\omega_z) = \exp(-\omega_z^2/\Delta^2)/(\Delta\sqrt{\pi})$ [34]. The dispersions Δ of the detuning and Ω_R of the Rabi frequency are the root-mean-square values of J_z and J_{\pm} respectively. Whereas J_z is dominated by fluctuations of \mathbf{I}_j symmetric about the dot centre, J_{\pm} is dominated by fluctuations antisymmetric in the $\tilde{\mathbf{E}}$ direction because $\tilde{\mathbf{E}} \cdot \nabla\psi_0(\mathbf{r})$ is odd with respect to the $\tilde{\mathbf{E}}$ projection of \mathbf{r} . Finally,

$$\Delta = \frac{A}{2\hbar}\sqrt{\frac{I(I+1)m\omega_0n_0}{2\pi\hbar d}}, \quad \Omega_R = \frac{e\tilde{E}A}{\hbar^2\omega_0}\sqrt{\frac{I(I+1)n_0}{8\pi d}}, \quad (2)$$

with $I = 3/2$ for GaAs, n_0 the nuclear concentration, and d the vertical confinement. It is seen that Ω_R is independent of B ; this is in contrast to EDSR mediated by the conventional $\mathbf{k} - \boldsymbol{\sigma}$ spin-orbit coupling, where Kramers' theorem requires that the Rabi frequency vanish linearly as $B \rightarrow 0$ [4, 35, 13].

In an instantaneous nuclear spin configuration with detuning $\delta\omega = 2\pi f - (\omega_L + \omega_z)$ and Rabi frequency Ω , the spin-flip probability from an initial \uparrow spin state is [36]:

$$p_{\downarrow}(\tau_{\text{EDSR}}) = \frac{\Omega^2}{(\delta\omega/2)^2 + \Omega^2} \sin^2 \left[\sqrt{(\delta\omega/2)^2 + \Omega^2} \tau_{\text{EDSR}} \right]. \quad (3)$$

(We neglect the electron spin relaxation and nuclear-spin dynamics, which remain slow compared with the Rabi frequency even in the EDSR regime [31, 32].) To compare with the time-averaged data of Figure 3, we average Equation (3) over ω_z with weight $\rho(\omega_z)$ and over Ω with weight $\rho(\Omega) = 2\Omega \exp(-\Omega^2/\Omega_R^2)/\Omega_R^2$. This latter distribution arises because the J_{\pm} acquire Gaussian-distributed contributions from both I_j^x and I_j^y components of the nuclear spins, hence it is two-dimensional. Averaging over ω_z and Ω results in a mean-field theory of the hyperfine-mediated EDSR. The resulting spin-flip probability

$$\bar{p}_{\downarrow}(\tau_{\text{EDSR}}; \Delta, \Omega_R) = \int_{-\infty}^{+\infty} d\omega_z \rho(\omega_z) \int_0^{+\infty} d\Omega \rho(\Omega) p_{\downarrow}(\tau_{\text{EDSR}}) \quad (4)$$

shows only a remnant of Rabi oscillations as a weak overshoot at $\tau_{\text{EDSR}} \sim \Omega_R^{-1}$. The absence of Rabi oscillations is characteristic of hyperfine-driven EDSR when the measurement integration time exceeds the nuclear evolution time [37], and arises because J_{\pm} average to zero.

4.1. Comparison with data

To compare theory and experiment, the probability $\bar{p}_\downarrow(\tau_{\text{EDSR}}; \Delta, \Omega_R)$ is scaled by a QPC sensitivity V_{QPC}^0 to convert to a voltage $\delta V_{\text{QPC}}^{\text{peak}}$. After scaling, numerical evaluation of Equation(4) gives the theoretical curves shown in Figure 3(a). The parameters that determine these curves are as follows: The Larmor frequency spread, $\Delta = 2\pi \times 28$ MHz, is taken as the quadrature sum of the jitter amplitude seen in Figure 2 and half the frequency modulation depth, whereas Ω_R and V_{QPC}^0 are numerical fit parameters. The 44 mT data (green curve in Figure 3(a)) give $\Omega_R = 1.7 \times 10^6$ s $^{-1}$ and $V_{\text{QPC}}^0 = 2.4$ μ V. Holding V_{QPC}^0 to this value, the 550 mT data give $\Omega_R = 1.8 \times 10^6$ s $^{-1}$ (blue curve in Figure 3(a)) and the 185 mT data give the dependence of Ω_R on microwave power P_{MW} shown in Figure 3(b). The Rabi frequency Ω_R increases as $\sqrt{P_{\text{MW}}}$ (Figure 3(b)) and is independent of B , both consistent with Equation (1). The B -independence of Ω_R — also evident in the EDSR intensity in Figure 2—and the absence of Rabi oscillations support our interpretation of hyperfine-mediated EDSR in the parameter range investigated.

Estimating $\hbar\omega_0 \sim 1$ meV [28], $\tilde{E} \sim 6 \times 10^3$ Vm $^{-1}$ at maximum applied power §, $d \sim 5$ nm, and using values from the literature $n_0 = 4 \times 10^{28}$ m $^{-3}$ and $A n_0 = 90$ μ eV [38] we calculate $\Omega_R \sim 11 \times 10^6$ s $^{-1}$, an order of magnitude larger than measured. The discrepancy may reflect uncertainty in our estimate of \tilde{E} .

Above, we generalized a mean-field description of the hyperfine interaction [39, 34] to the resonance regime. Justification for this procedure was provided recently in [32]. A distinctive feature of the mean-field theory is a weak overshoot, about 10 - 15%, that is expected in the data of Fig. 3(a) before $\delta V_{\text{QPC}}^{\text{peak}}(\tau_{\text{EDSR}})$ reaches its asymptotic value at $\tau_{\text{EDSR}} \rightarrow \infty$. No overshoot is observed in the 550 mT data (blue symbols in Figure 3(a)), which was taken in a parameter range where an instability of the nuclear polarization begins to develop; see Section 5. For the 44 mT data (green symbols in Figure 3(a)), a considerable spread of experimental points does not allow a specific conclusion regarding the presence or absence of an overshoot. The theory of [32] suggests that the existence of the overshoot is a quite general property of the mean-field theory. However, after passing the maximum, the signal decays to its saturation value vary fast, with Gaussian exponent $e^{-\Omega_R^2 \tau_{\text{EDSR}}^2}$. By contrast, the first correction to the mean-field theory decays slowly, as $1/(N\Omega_R^2 \tau_{\text{EDSR}}^2)$, where N is the number of nuclei in the dot. As a result, the two terms become comparable at $\tau_{\text{EDSR}} \sim \sqrt{\ln N}/\Omega_R$, which should make the maximum less pronounced. Because for $N \sim 10^5$ the factor $\sqrt{\ln N} \sim 3$, the corrections to the mean-field theory manifest themselves surprisingly early, at times only about $\tau_{\text{EDSR}} \approx 3/\Omega_R$, making the overshoot difficult to observe.

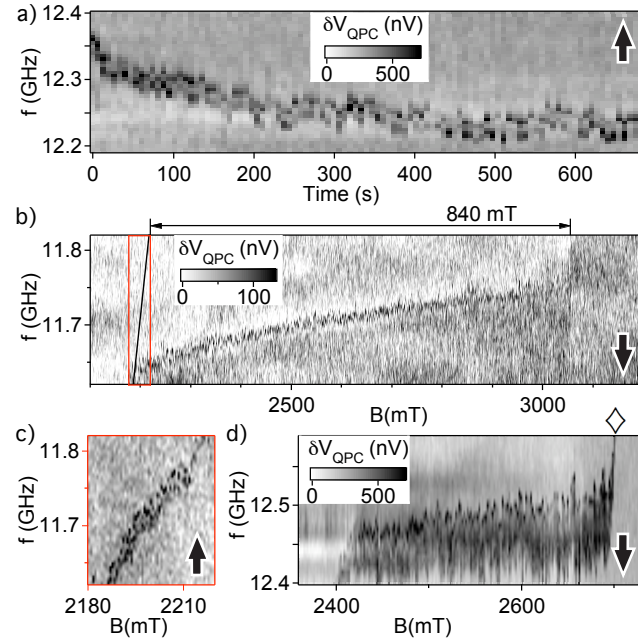


Figure 4. (a) Shift of the resonance frequency with time at constant $B = 2390$ mT, showing build-up of nuclear polarization over ~ 200 s. (b) A scheme to allow larger polarizations: the microwave frequency is repeatedly scanned over the resonance while B is swept upwards. Nuclear polarization partly counteracts B , moving the resonance away from its equilibrium position (black diagonal line) by up to 840 mT. (c) Similar data taken at lower microwave power and opposite frequency sweep direction, showing approximately the equilibrium resonance position. (Grey scale as in (b)). (d) Similar data as in (b), with faster sweep rate, showing more clearly the displacement and subsequent return to equilibrium of the resonance. \diamond marks the escape of the resonance from the swept frequency window. In all plots, arrows denote frequency sweep direction.

5. Nuclear polarization

Consistent with a hyperfine mechanism, this EDSR effect can create a non-equilibrium nuclear polarization [20]. If f is scanned repeatedly over the resonance at high power, a shift of the resonance develops (Figure 4(a)), corresponding to a nuclear spin alignment parallel to \mathbf{B} . The effect is stronger at higher B , and saturates over a timescale ~ 200 s. In Figure 4(b), we show how to build up a substantial polarization: While slowly increasing B , we scan f repeatedly downwards, i. e., in the direction which tracks the moving resonance. The resonance frequency remains approximately fixed, showing that the developing polarization compensates the increase in B . From the maximum line displacement from equilibrium, an effective hyperfine field of 840 mT can be read off, corresponding to a nuclear polarization of $\sim 16\%$. Figure 4(c) shows similar data

§ The maximum power is limited by non-resonant lifting of spin blockade, which we take to indicate a microwave amplitude exceeding the gate voltage from C to the nearest charge transition. The data in Figure 3(a) and the last data point in Figure 3(b) use power 2 ± 1 dB below this threshold, corresponding to 3.2 mV. Dropped uniformly across the whole device this voltage gives a field $\tilde{E} \sim 3 \times 10^3$ Vm $^{-1}$.

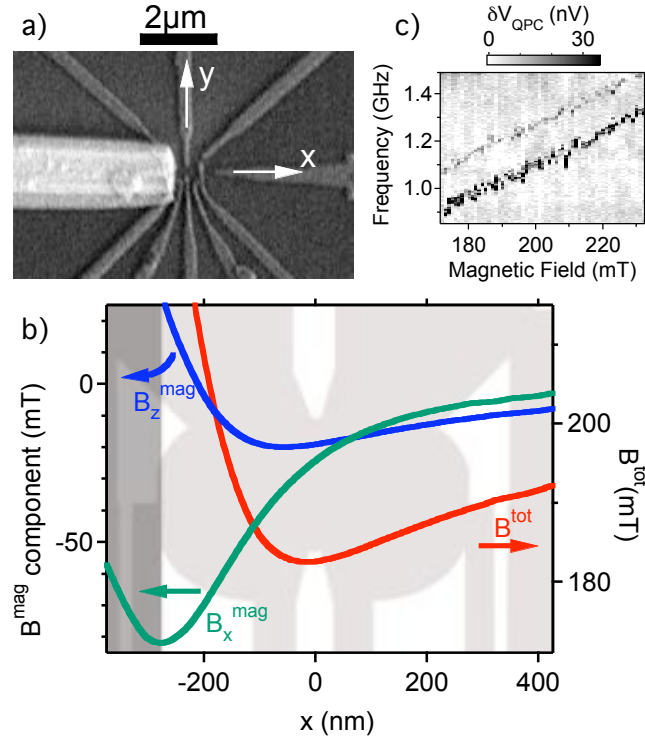


Figure 5. (a) A device similar to that of Figure 1, incorporating a micromagnet. (b) Total field magnitude B^{tot} (right axis) and the x and z components of the micromagnet contribution \mathbf{B}^{mag} (left axis), simulated at $y = 0$ for external field $B = 200$ mT along $\hat{\mathbf{z}}$ (out of the plane). B_y^{mag} vanishes by symmetry. The gate layout is shown in the background. (c) The associated split EDSR line. The lower resonance is stronger, as expected if the left electron is confined close to the minimum of B_{tot}

for lower power and opposite frequency sweep direction, indicating the approximate equilibrium line position. Figure 4(d), similar to Figure 4(b) but with a faster sweep rate, makes the displacement and eventual escape of the resonance clearer although the maximum polarization is less.

The resonance shift is observed to be towards lower frequency, corresponding to a nuclear polarization parallel to \mathbf{B} . This can be understood if the pulse cycle preferentially prepares the electron ground state T_+ over T_- , either because it is more efficiently loaded or because of electron spin relaxation. EDSR then transfers this electron polarization to the nuclei [21]. We emphasize that the line shift is opposite to what is given by the usual Overhauser mechanism for inducing nuclear polarization via electron resonance [40, 18].

6. Addressing individual spins

In quantum information applications, it is desirable to address individual spins selectively [5]. A scheme to allow this is presented in Figure 5. In an otherwise similar device (Figure 5(a)), we incorporated a 100 nm thick micron-scale permalloy (84% Ni,

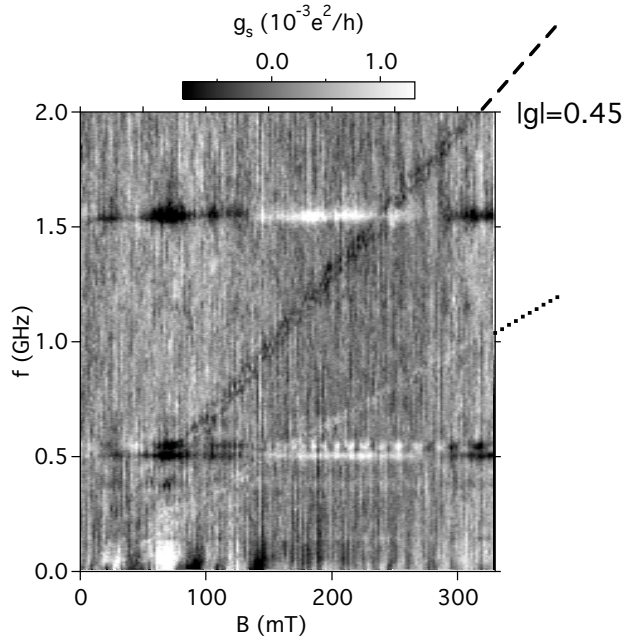


Figure 6. Spin resonance signal (measured in conductance) in the device of Figure 5(a). The EDSR signal shows up as a decrease in conductance as expected at frequency corresponding to $|g| = 0.45$ (marked with dashed line.) An additional signal of opposite sign appears at exactly half this frequency (dotted line). As in Figure 2, field- and frequency-independent backgrounds have been subtracted. The horizontal features at 0.5 and 1.5 GHz result from resonances of the microwave circuit.

16% Fe) magnet over 35 nm of atomic-layer-deposited alumina [12, 41]. This device was measured with external field \mathbf{B} normal to the heterostructure plane. A finite-element simulation of the field \mathbf{B}^{mag} due to the micromagnet, assuming complete permalloy magnetization along \mathbf{B} , yields the field profiles shown in Figure 5(b). The difference in total field $B^{\text{tot}} = |\mathbf{B} + \mathbf{B}^{\text{mag}}|$ between dots is ~ 7 mT. As expected, the EDSR line measured in this device is frequently split (Figure 5(c)). The splitting, 10 – 20 mT depending on precise gate voltage and pulse parameters, is not observed without the magnet and presumably reflects the field difference between dots. Since this splitting is considerably larger than the Overhauser field fluctuations, spins in left and right dots can be separately addressed by matching f to the local resonance condition [15].

7. Open issues and discussion

Finally, we discuss unexplained behavior observed only in the device of Figure 5(a). For the data described in this section, a simplified measurement scheme is used: Rather than applying gate pulses, the device is configured in the spin blockade region (point M in Figure 1(a)) throughout. Microwaves are applied continuously, and spin resonance is detected by directly measuring the QPC conductance g_s .

As well as the EDSR signal at full frequency $f = g\mu_B B/h$, an unexpected half-frequency signal is sometimes seen (Figure 6.) Furthermore, depending on the exact gate

configuration, both full-frequency and half-frequency signals can have either sign; the change in g_s at full frequency is usually negative as expected, but sometimes positive close to degeneracy of (1,1) and (0,2) charge configurations, where spin blockade is weakest [29]; by contrast, the change in g_s at half frequency is usually positive but sometimes negative far from degeneracy. For most gate configurations, full-frequency and half-frequency signals have opposite sign, as seen in Figure 6.

A half-frequency response is as far as we know unprecedented in spin resonance, and suggests second harmonic generation (SHG) from the microwave field. SHG is generally a non-linear phenomenon; it occurs for example in optical materials with non-linear polarizability [42] and in non-linear electronic components such as diodes. In our system, a hyperfine field at a harmonic of the microwave frequency arises if the confinement potential is non-parabolic.

However, SHG alone does not explain the sign of the conductance change seen at half-frequency in Figure 6. A positive signal could in principle be caused by an admixture of the (0,1) charge state; but it is observed even for the gate configurations where (0,1) is energetically inaccessible (in the top right of the spin blockade region of Figure 1(b)). Also, there is no reason why (0,1) should be admixed for one resonance but not the other. These anomalous behaviours are therefore left unexplained.

Acknowledgments

We acknowledge useful discussions with Al. L. Efros, H.-A. Engel, F. H. L. Koppens, J. R. Petta, D. J. Reilly, M. S. Rudner, J. M. Taylor, and L. M. K. Vandersypen. We acknowledge support from the DTO and from DARPA. E. I. R. was supported in part by a Rutherford Professorship at Loughborough University, U.K.

References

- [1] E. I. Rashba. *Sov. Phys. Sol. State.*, 2:1109, 1960.
- [2] R. L. Bell. *Phys. Rev. Lett.*, 9:52, 1962.
- [3] B. D. McCombe, S. G. Bishop, and R. Kaplan. *Phys. Rev. Lett.*, 18:748, 1967.
- [4] E. I. Rashba and V. I. Sheka. in *Landau Level Spectroscopy*, Elsevier, New York, 1991.
- [5] D. Loss and D. P. DiVincenzo. *Phys. Rev. A*, 57:120, 1998.
- [6] F. Jelezko et al. *Phys. Rev. Lett.*, 92:076401, 2004.
- [7] D. Rugar et al. *Nature*, 430:329, 2004.
- [8] M. Xiao et al. *Nature*, 430:435, 2004.
- [9] F. H. L. Koppens et al. *Nature*, 442:766, 2006.
- [10] S. I. Pekar and E. I. Rashba. *Sov. Phys. - JETP*, 20:1295, 1965.
- [11] Y. Kato et al. *Science*, 299:1201, 2003.
- [12] Y. Tokura et al. *Phys. Rev. Lett.*, 96:047202, 2006.
- [13] V. N. Golovach, M. Borhani, and D. Loss. *Phys. Rev. B*, 74:165319, 2006.
- [14] K. C. Nowack et al. *Science*, 318:1430, 2007.
- [15] M. Pioro-Ladrière et al. *Nature Physics*, 4:776, 2008.
- [16] E. A. Laird et al. *Phys. Rev. Lett.*, 99:246601, 2007.
- [17] H.-A. Engel and D. Loss. *Phys. Rev. Lett.*, 86:4648, 2001.

- [18] M. Gueron and Ch. Ryter. *Phys. Rev. Lett.*, 3:338, 1959.
- [19] M. Dobers et al. *Phys. Rev. Lett.*, 61:1650, 1988.
- [20] J. Baugh et al. *Phys. Rev. Lett.*, 99:096804, 2007.
- [21] M. Rudner and L. S. Levitov. *Phys. Rev. Lett.*, 99:246602, 2007.
- [22] M. Field et al. *Phys. Rev. Lett.*, 70:1311, 1993.
- [23] J. M. Elzerman et al. *Phys. Rev. B*, 67:161308, 2003.
- [24] R. Hanson et al. *Rev. Mod. Phys.*, 79:1217, 2007.
- [25] K. Ono et al. *Science*, 297:1313, 2002.
- [26] A. C. Johnson et al. *Phys. Rev. B*, 72:165308, 2005.
- [27] D. Goldhaber-Gordon et al. *Nature*, 391:156, 1998.
- [28] R. Hanson et al. *Phys. Rev. Lett.*, 91:196802, 2003.
- [29] F. H. L. Koppens et al. *Science*, 309:1346, 2005.
- [30] A. C. Johnson et al. *Nature*, 435:925, 2005.
- [31] J. R. Petta et al. *Science*, 309:2180, 2005.
- [32] E. I. Rashba. *Phys. Rev. B*, 78:195302, 2008.
- [33] L. S. Khazan, Yu. G. Rubo, and V. I. Sheka. *Phys. Rev. B*, 47:13180, 1993.
- [34] I. A. Merkulov, Al. L. Efros, and M. Rosen. *Phys. Rev. B*, 65:205309, 2002.
- [35] L. S. Levitov and E. I. Rashba. *Phys. Rev. B*, 67:115324, 2003.
- [36] I. I. Rabi. *Phys. Rev.*, 51:652, 1937.
- [37] D. J. Reilly et al. *Phys. Rev. Lett.*, 101:236803, 2008.
- [38] D. Paget et al. *Phys. Rev. B*, 15:5780, 1977.
- [39] A. V. Khaetskii, D. Loss, and L. Glazman. *Phys. Rev. Lett.*, 88:186802, 2002.
- [40] A. W. Overhauser. *Phys. Rev.*, 92:411, 1953.
- [41] M. Pioro-Ladrière et al. *Appl. Phys. Lett.*, 90:024105, 2007.
- [42] P. A. Franken et al. *Phys. Rev. Lett.*, 7:118, 1961.